Lattice Boltzmann simulation of the gas-solid adsorption process in reconstructed random porous media

L. Zhou,[1] Z. G. Qu,[1,*] T. Ding,[2] and J. Y. Miao[2]

[1]*MOE Key Laboratory of Thermal-Fluid Science and Engineering, School of Energy and Power Engineering, Xi'an Jiaotong University, Xi'an 710049, China*

[2]*Beijing Key Laboratory of Space Thermal Control Technology, Beijing Institute of Spacecraft System Engineering, Beijing 100094, China*

(Received 18 November 2015; revised manuscript received 5 February 2016; published 1 April 2016)

The gas-solid adsorption process in reconstructed random porous media is numerically studied with the lattice Boltzmann (LB) method at the pore scale with consideration of interparticle, interfacial, and intraparticle mass transfer performances. Adsorbent structures are reconstructed in two dimensions by employing the quartet structure generation set approach. To implement boundary conditions accurately, all the porous interfacial nodes are recognized and classified into 14 types using a proposed universal program called the boundary recognition and classification program. The multiple-relaxation-time LB model and single-relaxation-time LB model are adopted to simulate flow and mass transport, respectively. The interparticle, interfacial, and intraparticle mass transfer capacities are evaluated with the permeability factor and interparticle transfer coefficient, Langmuir adsorption kinetics, and the solid diffusion model, respectively. Adsorption processes are performed in two groups of adsorbent media with different porosities and particle sizes. External and internal mass transfer resistances govern the adsorption system. A large porosity leads to an early time for adsorption equilibrium because of the controlling factor of external resistance. External and internal resistances are dominant at small and large particle sizes, respectively. Particle size, under which the total resistance is minimum, ranges from 3 to 7 μm with the preset parameters. Pore-scale simulation clearly explains the effect of both external and internal mass transfer resistances. The present paper provides both theoretical and practical guidance for the design and optimization of adsorption systems.

DOI: 10.1103/PhysRevE.93.043101

I. INTRODUCTION

The mass transfer process in porous media is a widespread phenomenon that exists pervasively in the natural environment and manufacturing fields, such as in the geological transmission of petroleum and natural gas, blood flow in biological organisms, food processing, and coal combustion. A specific medium with a porous geometry exhibits several extraordinary features for the transport process. For instance, a species undergoes a tortuous route because of porous structures; the concomitant effects, such as flow resistance and heterogeneous mass distribution, should therefore be given close attention. If the species interacts with porous surfaces, the phase interface tends to induce an extra mechanism of action, which occurs in cases of dissolution, catalysis, etc. In addition, the species may still migrate inside the porous particles. Under this condition, the overall mass transfer performance is subject to both interparticle and intraparticle transfer characteristics.

A porous morphology has a significant effect on transport behavior. A proper simulation method must be employed to consider porous geometries accurately and effectively. Over the past decades, a novel and emerging mesoscopic approach, the lattice Boltzmann method (LBM), has shown excellent properties in the simulation of flow and mass transfer in porous media on the pore scale. Specifically, this method helps address complex geometry boundary conditions. The LBM has been applied to simulate transport phenomena in many cases, such as in packed beds [1–3], fuel cells [4], metallic foams [5], microreactors [6,7], chromatographic beds [8], composite membranes [9], shale structures [10], gas diffusion layers [11,12], and so on.

Simulations in porous media are conducted first from generating porous structures. Generally, geometric modeling methods can be categorized into experimental approaches and computer-based approaches. In experimental approaches, real geometric images are directly obtained with scanning technology, such as computer tomography [12–15], magnetic resonance imaging [3,16], scanning electron microscopy [4], and synchrotron microtomography [17]. Although imaging techniques can obtain actual geometrical morphologies, these methods are time consuming and expensive. Computer-based approaches generate and characterize porous morphologies on the basis of mathematical functions. The flexibility and changeability of digital reconstruction functions are advantageous in design and research. Hence, computational reconstruction methods are widely applied in the literature. Some popular methods include the defined particle group [6,7,18], Monte Carlo procedure [1,2], discrete element method [19], quartet structure generation set method [20,21], and other generation methods [11,22–26]. Geometric morphologies are mainly observed as regular particles (squares [21,22,27], circles [9,18,28], and spheres [1,2,8]) but should be presented as disordered random particles [14,20,24] as in actual cases.

In LBM simulations, the information on porous media is converted to different digital phase functions to distinguish fluid and solid phases. Furthermore, the boundary treatments of fluid-solid surfaces exert an essential influence on pore-scale simulations. A no-slip flow boundary is typically adopted for fluid-solid interactions. The frequently used treatments are the bounce-back-based schemes [1,2,5,16,17] because of their easy implementation. The nonequilibrium extrapolation [20,25] scheme is also considered as a robust method because of its second-order accuracy and stabilization. The research studies conducted on flow and mass transfer in multifarious porous media using LBM simulations are summarized in Table I for comparison purposes.

*zgqu@mail.xjtu.edu.cn

TABLE I. A review of existing studies on the LBM simulation of flow or mass transfer in multifarious porous media. The 2D and 3D means two dimensional and three dimensional. The SRT is the single–value–relaxation scheme. The MRT is the multirelaxation–time method. The TRT is the two–relaxation–time method. The references are listed in order of publication year.

Reference	Simulation case	Geometric modeling method	Geometric morphology	LB model	Boundary scheme of fluid-solid surface
[1]	Flow through bead packs	Standard hard-sphere Monte Carlo procedure	Random uniform spheres	3D SRT	Bounce back
[2]	Flow in fixed-bed reactors	Monte Carlo process	Randomly stacked spheres	3D SRT	Modified bounce back
[13]	Regeneration of diesel particulate filter	Computer tomography	Disordered random particles	3D SRT	Non-slip boundary
[16]	Packed bed reactors	2D confocal laser scanning microscopy, 3D magnetic resonance imaging	Disordered nonuniform particles	2D/3D SRT	Halfway bounce back
[14]	Flow in granular materials	X-ray computer tomography	Disordered irregular particles	3D SRT	Halfway bounce back
[11]	Gas diffusion layer of carbon paper	Stochastic generation method	Random fibers	3D MRT	Multireflection solid boundary
[4]	Solid oxide fuel cell anode	SEM micrograph image with IMAGEJ conversion	Random particles	2D SRT	Defined electrochemically boundary treatment modified from nonequilibrium bounce back for mass transfer
[22]	Fractal porous medium	Regular Sierpinski carpet generation	Ordered nonuniform squares	2D SRT	Bounce back
[27]	Heat recovery system	A random generator	Disordered uniform squares	2D MRT	Bounce back
[18]	Non-Darcy flow in porous media	Defined particle group	Disordered uniform circles	2D MRT	Halfway bounce back
[5]	Flow in metallic foam	Computer aided x-ray microtomography	Irregular foamlike	3D MRT	Full-way bounce back
[3]	Packed-bed reactors	Magnetic resonance imaging	Pellets of spheres, cylinders, and trilobe shaped	3D SRT	
[6]	Microreactor for hydrogen production	Defined particle group	Ordered uniform squares	2D SRT	No slip for flow; no flux for mass transfer
[7]	Hydrocarbon microreactors	Defined particle group	Disordered uniform squares	2D SRT	Nonequilibrium bounce back
[12]	Effective permeability, diffusivity of polymer electrolyte fuel cell gas diffusion layers	3D micrometer x-ray tomography	Random fibers	3D SRT	Halfway bounce back
[8]	Chromatographic beds	Experimental particle size distribution	Disordered nonuniform spheres	3D SRT	Halfway bounce back
[19]	Packed beds	Discrete element method	Disordered uniform spheres	3D TRT	Bounce back
[28]	Flow in porous media	Defined particle group	Ordered uniform circles	2D SRT	On-site interpolation-free scheme
[23]	Permeability of cementitious materials	HYMOSTRUC3D generation model	Voxels containing capillary pores, circles, and random particles	3D MRT	Halfway bounce back
[17]	Inertial flow in sphere packs	3D synchrotron microtomography image	Irregular pack of uniform spheres	3D SRT	Standard bounce back
[24]	Dissolution and precipitation	Stochastic nucleation and growth algorithm	Disordered random particles	2D SRT	Bounce back
[25]	Diffusion in porous media	Voronoi geometry generation algorithm	Randomly connected channels with large pores embedded	2D TRT	Nonequilibrium extrapolation with spatial interpolation

TABLE I. (*Continued*).

Reference	Simulation case	Geometric modeling method	Geometric morphology	LB model	Boundary scheme of fluid-solid surface
[20]	Volatile organic compound (VOC) transport in porous materials	Quartet structure generation set method	Disordered random particles	3D SRT	Nonequilibrium extrapolation
[9]	Composite membranes	Sphere-based simulated annealing method	Disordered uniform circles	2D SRT	Bounce back
[21]	Diffusion in porous media	Quartet structure generation set method	Disordered uniform squares	2D SRT	Interpolation and bounce back
[15]	Flow in porous media	Microcomputed tomography scanned images	Disordered nonuniform particles	3D MRT	Halfway bounce back
[26]	Gas diffusion in porous media	Fractional Brownian motion model	Stochastic fractal particles	2D SRT	
[10]	Shale transport properties	Markov chain Monte Carlo method	Disordered nonuniform particles	3D MRT	No slip for flow; no flux for mass transfer

The standard LBM scheme is originally fit for the hydrodynamic physics with the near-incompressible limit. Meanwhile, the direct-simulation feature makes this approach attractive in complex hydraulic properties in porous media, such as turbulence and compressible fluids. Hitherto, some improvement works have been devoted to increase the numerical stability and accuracy issues especially at high Reynolds and moderately high Mach numbers, for instance, the multiple-relaxation-time (MRT) model [29–31], the regularization method [32–34], the entropic method [34–36], and the selective viscosity model [37]. The MRT model introduces a collision matrix to perform the collision process in the momentum space. The regularization technique is implemented for the precollision distribution functions in terms of the local density, velocity, and momentum flux tensor. The entropic stabilizer is based on such a philosophy that the optimal states are constructed by maximizing the entropy under pertinent constraints. The selective viscosity model applies low-pass filters on distribution functions to remove the high frequency oscillations that are related to numerical instabilities. Stability analyses have been performed to verify that through those optimization techniques, dispersion or dissipation relations are enhanced and the numerical stability is improved.

Despite the growing application of the LBM approach in transport processes in porous media, only a few studies have explored the adsorption process, which is a typical surface-based mass transfer reaction involving fluid adsorbates and solid adsorbents. Manjhi *et al.* [38] and Verma *et al.* [39] explored the problems on gas-solid adsorption in porous media using the LB scheme. Mean porosity was introduced to consider the effect of porous features. Levesque *et al.* [40] applied the LB scheme with consideration of adsorption and desorption to calculate two mesoscale dynamical properties of tracers in heterogeneous media. Their work centered on the dependence of the dynamical properties of tracers on tracer-surface affinity. As the adsorption and desorption processes were introduced as instances for tracer-surface affinity, adsorption characteristics were not discussed in detail. Zhou *et al.* [41] employed the LB model to conduct dynamic adsorption processes in ordered porous media. The results were verified with analytical solutions and literature results.

To date, little attention has been paid to the influence of stochastic geometric morphologies on adsorption on the pore scale. The purpose of the present study is to explore the dynamic adsorption processes in disordered random adsorbent particles with different porous features. First, different two-dimensional (2D) stochastic porous structures are generated to act as the adsorption system. Then, LB evolution solutions are employed to achieve fluid flow and mass transport in the adsorption system. Adsorption processes in reconstructed media are simulated with consideration of interparticle, interfacial, and intraparticle mass transfer characteristics. The effects of porosity and particle size on three mass transfer segments are discussed in detail.

II. PHYSICAL AND MATHEMATICAL MODELS

A. Physical formulation and morphology reconstruction

The simulated physical case is the gas-solid adsorption process in a 2D channel filled with disordered random porous media. Figure 1 shows the schematic of the detailed mass

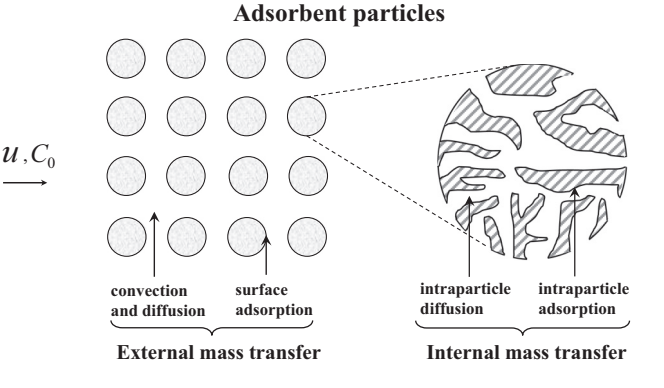

FIG. 1. Schematic of the adsorption process in a channel filled with circular adsorbent particles.

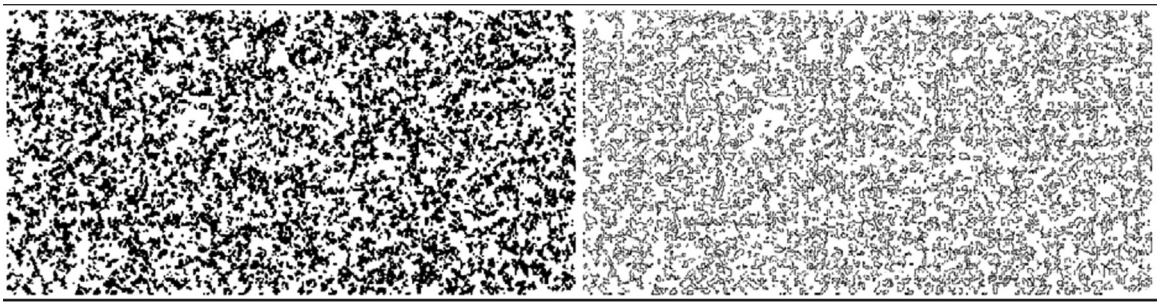

(a) (b)

FIG. 2. Disordered random porous media reconstructed with the QSGS and BRCP (a) the phase image and (b) the boundary recognition. The domains are 1008 × 520 lattice units in size.

transport in the adsorption process. A typical adsorbent particle is simplified as a circle for simplicity, and the enlarged image presents the internal (intraparticle) mass transport. The gas adsorbate flows through the porous domain from left to right. The adsorbate is transferred to adsorbent particle surfaces via external bulk convection and diffusion. Through surface adsorption, the adsorbate is then adsorbed on the external surfaces of the particle. The adsorbate further diffuses into the micropores inside the adsorbent through intraparticle diffusion. Finally, intraparticle adsorption is achieved when the diffused adsorbate inside is further adsorbed on the surfaces of the micropores. It is worth mentioning that the intraparticle convection can be ignored due to the nanoscale feature of internal pores. Thus, the internal mass transport rate is limited by the intraparticle diffusion and can be described by the effective diffusion coefficient based on the solid diffusion theory [42].

An adsorption system is filled up with numerous particles with various geometric morphologies. This system with disordered random porous media is generated via computerized image reconstruction, which is a convenient and efficient method for realizing different porous characteristics. The quartet structure generation set (QSGS) [43] is employed. Four parameters, namely, core distribution probability, directional growth probability, phase interaction growth probability, and phase volume fraction, are identified to control the internal morphological features of the granular media. The porosity and particle size are controlled by the phase volume fraction and core distribution probability, respectively.

The interfacial adsorption reaction is a kinetic mass transfer process in which the mass transport is described by the interfacial concentration gradient. The gradient requires the identification of the normal direction to the interfacial node [44]. All the interfacial nodes should be recognized and then classified into different types to easily determine the normal direction. Hence, a universal boundary recognition and classification program (BRCP) for porous media is developed in FORTRAN. The procedures are described below.

(a) Read into the data information of the phase functions of the porous media generated by the QSGS method. Here, the solid phase is set to "1," and the void phase is set to "0."

(b) Double the grid numbers. The geometry is enlarged by the multiple of 2, and the grid resolution is doubled. This treatment is conducive to excluding the fewest number of unexpected boundary nodes in following steps (c)–(e). Meanwhile, it is contributive to improving the grid resolution and the computational accuracy.

(c) Recognize the boundary nodes. If a solid node has at least one void phase node as its adjacent point, then this solid node is marked as a boundary node.

(d) Exclude the unexpected boundary nodes that have little contribution to the porous simulation. These nodes include the isolated nodes and nodes within a separate line. The excluded boundary nodes are marked as void nodes.

(e) Repeat steps (c) and (d) until the results of the boundary recognition remain the same. Figure 2 illustrates one case of the processed phase image and boundary recognition result after the implementation of steps (a)–(e). The postprocessed domains are 1008 × 520 lattice units (lus) in size.

(f) After the completion of the boundary recognition, classify all the boundary nodes into 14 types, i.e., four flat wall nodes, four convex corner nodes, four concave corner nodes, and two convex-to-convex nodes. Figure 3 presents an illustration of the 14 types of boundary nodes. Flat wall nodes (B1–B4) are within a straight-line boundary. Convex nodes (B5–B8) and concave nodes (B9–B12) are observed at the points of intersection between two straight-line boundaries. Convex-to-convex nodes (B13 and B14) represent the intersection points of four straight-line boundaries.

For all the types of boundary nodes, the boundary conditions are the same in the adsorption system. The only distinction among them is the neighborhood of each one.

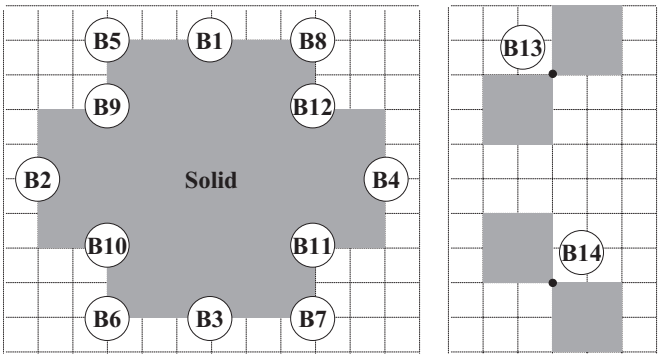

FIG. 3. Illustration of the 14 types of boundary nodes, namely, four flat wall nodes (B1)–(B4), four convex corner nodes (B5)–(B8), four concave corner nodes (B9)–(B12), and two convex-to-convex nodes (B13)–(B14).

TABLE II. Structure parameters for the reconstructed porous media under different porosities and the same average particle size. The particle size and specific surface area are expressed in lattice units.

Structure name	$P1$	$P2$	$P3$	$P4$
Porosity ε	0.494	0.580	0.665	0.766
Average particle size d_p	46.92	46.66	46.24	46.55
Specific surface area s_v	0.1279	0.1286	0.1298	0.1317

Specifically, the adjacent point on the normal direction of every type of boundaries can be determined according to the boundary classification to implement the Langmuir kinetics. The aforementioned BRCP approach is not only applicable to computerized image reconstruction, but also applicable to experimental scanned images whose solid and void phases are marked differently.

To investigate the influence of porous morphological features on adsorption properties, two groups of porous structures are reconstructed: one group has different porosities with the same particle size, whereas the other group has different particle sizes with identical porosity. Porosity ε refers to the fraction of the area of voids over the total area of the domain. The average particle size d_p is calculated with Eq. (1) [45,46],

$$d_p = 6/s_v, \tag{1}$$

where s_v is the specific surface area, that is, the ratio of the length of the total boundary lines to the total area of the domain [45]. The morphological features of the reconstructed porous structures in the two groups are listed in Tables II and III, respectively. The structures are named Pn or Dn, where n is a serial number, P denotes porosity, and D denotes particle size. The particle size and specific surface area are given in lattice units. The domains all measure 1008×520 lattice units in size.

B. Mathematical formulation

1. Governing equation

The pore-scale simulation of the adsorption system includes three governing equations for the mass transport of interparticle, interfacial, and intraparticle segments. The governing equation of interparticle mass transfer is

$$\frac{\partial C}{\partial t} + u\frac{\partial C}{\partial x} + v\frac{\partial C}{\partial y} = D_s\left(\frac{\partial^2 C}{\partial x^2} + \frac{\partial^2 C}{\partial y^2}\right). \tag{2}$$

An adsorption reaction occurs when the adsorbate comes into contact with the external surface of the solid adsorbent particle. The interfacial mass transfer mechanism is described with the typical Langmuir adsorption kinetics given by

$$D_s\frac{\partial C}{\partial \boldsymbol{n}} = \frac{\partial N}{\partial t} = k_1 C(N_m - N) - k_{-1}N. \tag{3}$$

In this equation, k_1 and k_{-1} are the adsorption and desorption rate constants, respectively. C is the gas concentration on the solid surface. N is the adsorbed phase amount, and N_m is the saturation adsorbed amount. As shown in Eq. (3), the adsorbed amount on the interfaces is obtained with the following relation:

$$N_{(t+1)} - N_{(t)} = \Delta t[k_1 C(N_m - N) - k_{-1}N]. \tag{4}$$

The intraparticle mass transport is treated using the homogeneous solid diffusion model [42], which is shown as

$$\frac{\partial N}{\partial t} = D_{sp}\left(\frac{\partial^2 N}{\partial x^2} + \frac{\partial^2 N}{\partial y^2}\right), \tag{5}$$

where D_{sp} is the solid diffusion coefficient inside the particles. The flow and concentration boundary conditions are described in Table IV.

2. LB approach

Considering the numerical stability and accuracy, this paper adopts the popular MRT model with the $D2Q9$ scheme for the flow simulation. The evolution equation is written in the following linear formulation (containing collision and streaming steps) [47]:

$$\begin{aligned}&\boldsymbol{f}(\boldsymbol{r}_i + \Delta t\ \boldsymbol{e}_i, t + \Delta t) - \boldsymbol{f}(\boldsymbol{r}_i, t)\\ &\quad = -\boldsymbol{M}^{-1}\hat{\boldsymbol{S}}[\boldsymbol{m}(\boldsymbol{r},t) - \boldsymbol{m}^{\mathrm{eq}}(\boldsymbol{r},t)].\end{aligned} \tag{6}$$

$\boldsymbol{e}_i$ is the discretized velocity direction. The boldface symbol represents a matrix. $\boldsymbol{f}$ is a column vector expressing the nine velocity distribution functions. $\boldsymbol{M}$ is a nine-order matrix that transforms the velocity distribution functions $\boldsymbol{f}$ to the velocity moments $\boldsymbol{m}$ through the following linear mapping:

$$\boldsymbol{m} = \boldsymbol{M}\cdot\boldsymbol{f} \quad \text{or} \quad \boldsymbol{f} = \boldsymbol{M}^{-1}\cdot\boldsymbol{m}. \tag{7}$$

The elements of matrix $\boldsymbol{M}$ can be found in Ref. [47]. The velocity moments $\boldsymbol{m}$ are expressed as

$$\boldsymbol{m} = (\rho, e, \varepsilon, j_x, q_x, j_y, q_y, p_{xx}, p_{xy})^T. \tag{8}$$

The format of the nine equilibrium moments $\boldsymbol{m}^{\mathrm{eq}}$ is described in Ref. [47]. $\hat{\boldsymbol{S}}$ is the nine-order diagonal collision matrix of relaxation rates that is written in compact notation as

$$\hat{\boldsymbol{S}} = \mathrm{diag}(s_\rho, s_e, s_\varepsilon, s_j, s_q, s_j, s_q, s_v, s_v). \tag{9}$$

TABLE III. Structure parameters for reconstructed porous media under different average particle sizes and the same porosity. The particle size and specific surface area are expressed in lattice units.

Structure name	$D1$	$D2$	$D3$	$D4$	$D5$	$D6$	$D7$	$D8$
Porosity ε	0.720	0.722	0.724	0.722	0.724	0.722	0.719	0.721
Average particle size d_p	9.69	14.82	20.86	25.72	35.48	43.25	52.08	64.55
Specific surface area d_p	0.6194	0.4048	0.2876	0.2333	0.1691	0.1387	0.1152	0.0929

TABLE IV. Boundary conditions of the adsorption process in porous structures. L and H are the domain length and height, respectively. $u_{\max}$ is the maximum velocity of the parabolic velocity profile.

Position	Flow	Concentration
Inlet	Parabolic velocity profile: $u(y) = -4u_{\max}y(y-H)/H^2$	Constant concentration: C_0
Outlet	Fully developed flow: $u_L = u_{L-1}, v_L = v_{L-1}$	No concentration flux: $\frac{\partial C}{\partial x} = 0$
Upper and bottom	Nonslip: $u = v = 0$	No concentration flux: $\frac{\partial C}{\partial y} = 0$
Particle surfaces	Nonslip: $u = v = 0$	Langmuir adsorption reaction: $D_s\frac{\partial C}{\partial \boldsymbol{n}} = k_1 C(N_m - N) - k_{-1}N$

The criterion of the range of values s_i is described in Refs. [30,31,48]. The present study sets the values as

$$s_\rho = s_j = 1.0, \quad s_e = s_\varepsilon = 1.1, \quad s_q = 8\frac{2-s_\upsilon}{8-s_\upsilon}. \tag{10}$$

Moreover, the relaxation rate s_υ is related to the kinetic viscosity υ by the following format:

$$s_\upsilon = 2/(1+6\upsilon). \tag{11}$$

According to the physical processes in Fig. 1, the convection effect, which is ignored inside particles, exists only among particles. The adsorption reaction only occurs when the adsorbate contacts the particles, and it does not exist in the bulk fluid. Hence, it is assumed that the interparticle adsorbate transport does not affect the local velocity. Based on this decoupled relation, the intraparticle mass transport is performed by the passive-scalar concentration. Compared with the collision matrix in the MRT model, the single-relaxation-time (SRT) scheme is contributive to improving the computational efficiency. Furthermore, with the passive-scalar feature, the 2D lattice directions can be reduced from 9 to 5 without accuracy loss for mass transport [6,16]. Thus, the $D2Q5$ model is adopted for the interparticle mass transport, described as

$$g_i(\boldsymbol{r}+\Delta t\ \boldsymbol{e}_i, t+\Delta t) - g_i(\boldsymbol{r},t) = -\frac{1}{\tau_s}\left[g_i(\boldsymbol{r},t) - g_i^{\mathrm{eq}}(\boldsymbol{r},t)\right]. \tag{12}$$

g_i is the concentration distribution function, and τ_s is the relaxation time. The equilibrium distribution function g_i^{eq} is expressed as

$$g_i^{\mathrm{eq}}(\boldsymbol{r},t) = C_s w_i\left(1 + \frac{\boldsymbol{e}_i\cdot\boldsymbol{u}}{c_s^2}\right). \tag{13}$$

w_i is the weight coefficient. For the $D2Q5$ model, $w_0 = 1/3$, and $w_{1\text{–}4} = 1/6$. c_s denotes the sound speed, which is $1/\sqrt{3}$ for the $D2Q5$ scheme.

The mass diffusion coefficient is obtained by

$$D_s = c_s^2(\tau_s - 0.5)\Delta t, \tag{14}$$

and the concentration of s species is obtained from

$$C_s = \sum_i g_i. \tag{15}$$

Based on the homogeneous solid diffusion theory [42] in Eq. (5), the mass transfer inside adsorbent particles is also modeled with the $D2Q5$ scheme with the zero velocity. The solid diffusion coefficient D_{sp} is realized with a different relaxation time from that of interparticle mass transport.

The boundary treatment plays an essential role in simulating flow and surface-based mass transfer in porous media. Here, the nonequilibrium extrapolation method proposed by Guo *et al.* [49] is applied to the hydrodynamic boundary conditions of both the channel domain boundaries and the fluid-solid surfaces. For the mass transfer problem, the unknown concentration distribution function is obtained from the sum of all the unknown functions and distributed by the weight coefficients [50] in Eq. (16),

$$g_{i(\boldsymbol{e}_i\cdot\boldsymbol{n}>0)} = \frac{\left[C_w - \sum_{i(\boldsymbol{e}_i\cdot\boldsymbol{n}\leqslant 0)} g_i\right]w_i}{\sum_{i(\boldsymbol{e}_i\cdot\boldsymbol{n}>0)} w_i}, \tag{16}$$

where $\boldsymbol{n}$ is the normal direction of the boundary node. The key issue is determining the boundary concentration C_w. According to the boundary settings in Table IV, inlet C_w is known and naturally determined. As for the concentration flux condition, the accurate three-point finite-difference scheme as shown in Eq. (17) is introduced to match with the concentration gradient,

$$\frac{\partial C_w}{\partial \boldsymbol{n}} = \frac{3C_w - 4C_{(j,n+1)} + C_{(j,n+2)}}{2\ \Delta n}. \tag{17}$$

For the outlet, the upper and bottom walls, $\frac{\partial C_w}{\partial \boldsymbol{n}}$, are zero directed by the no concentration flux condition. At the fluid-solid interfaces, Eq. (17) is coupled with the Langmuir kinetic adsorption reaction in Eq. (3) to solve C_w.

III. MODEL VERIFICATION

The applicability and accuracy of the LBM for the adsorption system were validated in our previous work [41]. In Ref. [41], the adsorption system is simplified as regular arrangements of the same square particles. The present study focuses on the impact of stochastic geometric morphologies on the dynamic adsorption processes. It is necessary to verify the flow property accompanied by complex boundary nodes.

In essence, the lattice Boltzmann equation is a kinetic model based on a special discretization scheme of the continuous Boltzmann equation. The entire velocity space is replaced by the finite velocity directions, such as through the Hermite expansions [51–54]. For the 2D space, the $D2Q9$ scheme is second order and suffers from third-order errors in the momentum balance equation [51–54], being unable to retrieve second-order nonequilibrium moments and third-order equilibrium moments without errors. Higher-order models improve the prediction accuracy with requirement of more discrete velocities, such as the $D2Q13$, $D2Q17$, and $D2Q25$, and so on [52,53]. However, the implementation with increased velocity directions became difficult for porous media with

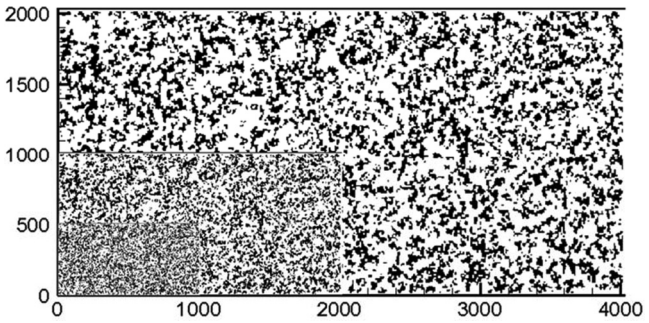

FIG. 4. Diagram of three porous media with different resolutions by scaling structure $D1$ two and four times.

reduced computational efficiency. The $D2Q9$ scheme has been successfully applied for the fluid flow simulation with low velocity, Reynolds and Mach numbers as indicated in Refs. [6,7,16,18,28]. For the sake of reducing the numerical errors, the Reynolds ($d_p u/\upsilon$) and Mach (u/c_s) numbers are confined smaller than 0.06 and 0.002, respectively, which is exactly consistent with the fact that the weak flow is always present in the adsorption system.

The simulation for random porous media requires adequate grid resolution, so the numerical convergence is first researched. The structure $D1$ with the minimum average particle size as 9.69 lu is enlarged by two and four times, respectively, resulting in three investigated structures with different resolutions. These three checked structures are shown in Fig. 4. The tortuosity, an intrinsic property of a porous structure related to the whole porous morphology, is adopted as the comparison parameter [25]. Since low Reynolds ($\mathrm{Re} = d_p u_{\max}/\upsilon$) flow is usually present in the adsorption system, a constant $\mathrm{Re} = 0.06$ is preset at the inlet under the flow boundary conditions in Table IV. In simulation, the kinetic viscosity υ is kept as $1/6$, and the velocity $u_{\max}$ changes with different d_p of the three media. As the flow reaches the steady state, the tortuosity τ_t can be obtained with Eq. (18) [55,56],

$$\tau_t = \frac{\sum_{(i,j)} U_{\mathrm{mag}}(i,j)}{\sum_{(i,j)} |U_x(i,j)|}. \tag{18}$$

U_x is the velocity component in the leading flow direction, and U_{mag} is the velocity magnitude of the fluid lattice node (i,j) calculated as

$$U_{\mathrm{mag}}(i,j) = \sqrt{u^2_{(i,j)} + v^2_{(i,j)}}. \tag{19}$$

The structure parameters and predicted tortuosity of three media are presented in Table V. With the increased resolution, the tortuosity differs little from each other. Therefore, particles

TABLE V. Structure parameters and tortuosity results of the three media in Fig. 4

Area	Average particle size d_p	Porosity ε	Tortuosity τ_t
1008×520	9.69	0.720	1.3200
2016×1040	19.37	0.720	1.3208
4032×2080	38.74	0.720	1.3207

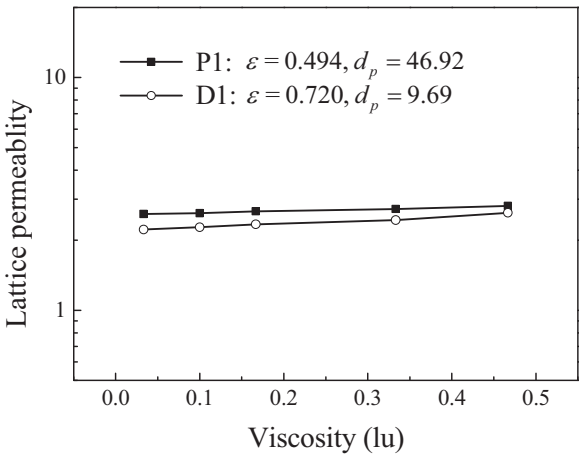

FIG. 5. The permeability-viscosity relation for structures $P1$ and $D1$.

under the average characteristic size as 9.69 lu are feasible for low Reynolds numbers. For higher Reynolds numbers in porous media flows, higher particle sizes in terms of lattice units are required for implementation.

The second validation study is for the viscosity dependence of the computed permeability. This dependence has been extensively reported in the literature, especially for the single-relaxation-time (SRT) model in which the bulk and boundary errors are related to powers of the kinematic viscosity [57,58]. Permeability is an inherent feature of porous media and describes the hindering effect of the porous morphology on fluid flow. For low Reynolds flow, the permeability can be obtained from Darcy' law, defined as

$$k = -\frac{\bar{u}\mu}{\nabla p}. \tag{20}$$

μ is the dynamic viscosity. $\bar{u}$ is the average streamwise velocity. ∇p is the streamwise pressure gradient, which is calculated as $\nabla p = \nabla \rho c_s^2$ in lattice units. The structures $P1$ and $D1$ with minimum porosity (0.494) and particle size (9.69 lu), respectively, are selected to compute permeability. The known pressure is prescribed at the inlet and outlet ($p_{\mathrm{inlet}} > p_{\mathrm{outlet}}$), and periodic boundary conditions are set for the upper and bottom walls. Five different kinetic viscosities are simulated, and the permeability-viscosity relations are shown in Fig. 5. With the MRT scheme, the permeability is weakly dependent on the viscosity, which is consistent with the results in literature [23,59,60]. In addition, the minimum porosity and average particle size are 0.494 and 9.69 lu for the present reconstructed media, respectively. Such parameters can naturally avoid the problem of viscosity dependent permeability.

Under the condition of low pore size and porosity, this problem may be severe. If the lattice characteristic length is small, the resolution of the porous morphology falls into low discretization levels, and the low-discretization effect cannot be completely eliminated when investigating stochastic porous media [60]. As the porosity decreases, the primary source of numerical error, which is resulted from the boundary between solid and pore, is accordingly increased. Some significant improvements with accurate no-flow boundary treatments have

been reported to suppress this problem of viscosity independent permeability [61]. These improved methods include the linearly and quadratic interpolated bounce-back scheme [62–64], the multireflection approach [48], and the technique with a parametrization of the free relaxation parameter [57,58].

IV. RESULTS AND DISCUSSION

The effects of the interparticle, interfacial, and intraparticle mass transfer performances on the overall characteristics of dynamic adsorption processes are investigated. The two generated groups of random porous structures in Tables II and III are simulated. The inlet and outlet are extended with 100 and 120 additional lattice units, respectively, for the implementation of the specified boundary conditions.

In the LB simulations, the variables are nondimensional lattice quantities. The conversion from physical world units to lattice units could be realized on the basis of the same dimensionless criterion numbers. Table VI introduces the relevant parameters with physical units and dimensionless lattice units for the adsorption simulation. This table also shows the scaling relation between the physical and lattice units. The symbol " ˆ " stands for physical parameters. Water vapor and silica gel are selected as the adsorbate and adsorbent, respectively.

The adsorption reaction process is an unsteady system. In every simulation step of the LBM, a mass transport procedure is performed from the interparticle transfer to the interfacial one and then to the intraparticle segment. The three mass transfer segments are coupled to one another. The adsorption equilibrium state of the system is achieved when each mass transport process is conducted completely.

A. Performance indices for mass transport

The mass transfer resistance includes the external and internal resistances as shown in Fig. 1. External resistance is derived from the interparticle and interfacial mass transfer processes. The efficiency of the interparticle mass transfer process is related to the extent of the convection-diffusion in the bulk fluid. It is evaluated with the permeability of the porous structure and the interparticle transfer coefficient of the adsorbate in the porous media. The interfacial mass transport process is related to the adsorbate concentration at the interfaces. Hence, this process is dependent on the interparticle mass transfer performance. Internal resistance is derived from the intraparticle mass transport process and is controlled by intraparticle diffusion. Thus, internal resistance is determined by particle size. The respective performance indices are employed to account for the property of each mass transfer segment.

Permeability is an intrinsic property of the porous media, and obtained from Eq. (20) according to the procedure in Sec. III. The interparticle transfer coefficient characterizes the transport level of the adsorbate in bulk fluid. This parameter can be directly measured from the LB simulation with the Eq. (21) as suggested in Chen *et al.* [65],

$$D_{\text{trans}} = \frac{D_s\left(\int_0^H \frac{\partial C}{\partial x} dy\right)/H}{(C_{\text{in}} - C_{\text{out}})/L}. \tag{21}$$

In Eq. (21), C_{in} and C_{out} are obtained from the average adsorbate concentration at the inlet and outlet, respectively. The interparticle transfer coefficient D_{trans} includes the overall effect of the convection, interparticle diffusion, and interfacial adsorption reaction on the interparticle transport extent during the unsteady adsorption process.

The interfacial mass transfer property is evaluated with the transients of the average values of the dimensionless adsorbed amount of all the particle surfaces, which are given by $\overline{N}_{\text{surf}(t)}$ and calculated as

$$\overline{N}_{\text{surf}(t)} = \left.\frac{\sum_i \sum_j N_{(t)(i,j)}}{\sum_i \sum_j N_m}\right|_{(i,j)\in\text{interface}}. \tag{22}$$

$N_{(t)(i,j)}$ is the adsorbed phase amount of point (i, j) at time t.

The intraparticle mass transport performance can be revealed by the transients of the overall average values of the dimensionless adsorbed amount $\bar{N}_{\text{tot}(t)}$ as expressed in

TABLE VI. Physical parameters and dimensionless lattice units for the adsorption simulation. The symbols with ˆ are the physical parameters. The adsorbate gas is selected as the water vapor with a density of 0.58 kg m^{-3}, and silica gel is selected as the adsorbent with a density of 670 kg m^{-3}. $\Delta\hat{n}_s/\Delta\hat{x}^3$ and $\Delta\hat{n}_z/\Delta\hat{x}^3$ denote the molar concentrations of the gas concentration and adsorbed amount, respectively.

Parameter	Physical symbol	Physical value	Lattice symbol	Lattice value	Scaling relation
Sound speed	$\hat{c}_s$	340.40 m s^{-1}	c_s	$1/\sqrt{3}$	$u_r = \hat{c}_s/c_s$
Domain length	$\hat{L}$	2.456×10^{-4}m	L	1228	$L_r = \hat{L}/L$
Domain height	$\hat{H}$	1.040×10^{-4}m	H	520	$L_r = \hat{H}/H$
Grid step	$\Delta\hat{x}(\Delta\hat{y})$	2×10^{-7} m	$\Delta x(\Delta y)$	1	$\Delta\hat{x} = L_r\Delta x$
Time step	$\Delta\hat{t}$	3.40×10^{-10} s	Δt	1	$\Delta\hat{t} = \Delta t\ L_r/u_r$
Gas density	$\hat{\rho}$	0.58 kg m^{-3}	ρ	1	$\hat{\rho}_s = \rho_s\Delta\hat{m}/\Delta\hat{x}^3$
Kinematic viscosity	$\hat{\upsilon}$	2.01×10^{-5} m^{2}s^{-1}	υ	1/6	$\hat{\upsilon}_f = \upsilon_f\Delta\hat{x}^2/\Delta\hat{t}$
Inlet gas velocity	$\hat{u}_{\max}$	0.0589 m s^{-1}	$u_{\max}$	0.0001	$\hat{u}_{\max} = u_{\max}\Delta\hat{x}/\Delta\hat{t}$
Inlet gas concentration	$\hat{C}_0$	32.22 mol m^{-3}	C_0	10	$\hat{C}_0 = C_0\Delta\hat{n}_s/\Delta\hat{x}^3$
Gas diffusion coefficient	$\hat{D}_s$	2.01×10^{-5} m^2 s^{-1}	D_s	1/6	$\hat{D}_s = D_s\Delta\hat{x}^2/\Delta\hat{t}$
Solid diffusion coefficient	$\hat{D}_{sp}$	4.02×10^{-8} m^2 s^{-1}	D_{sp}	1/3,000	$\hat{D}_{sp} = D_{sp}\Delta\hat{x}^2/\Delta\hat{t}$
Saturation adsorption amount	$\hat{N}_m$	11166 mol m^{-3} (0.30 kg kg^{-1})	N_m	3	$\hat{N}_m = N_m\Delta\hat{n}_z/\Delta\hat{x}^3$
Adsorption rate constant	$\hat{k}_1$	9.13×10^8 m^3 mol^{-1} s^{-1}	k_1	0.005	$\hat{k}_{-1} = k_{-1}/\Delta\hat{t}(\Delta\hat{n}_s/\Delta\hat{x}^3)$
Desorption rate constant	$\hat{k}_{-1}$	2.90×10^6 s^{-1}	k_{-1}	0.001	$\hat{k}_{-1} = k_{-1}/\Delta\hat{t}$

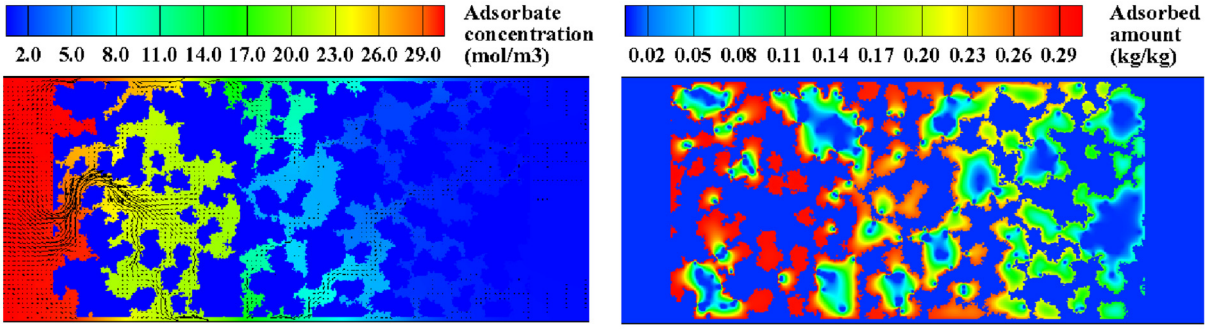

(a) Structure $P1$: ε =0.494

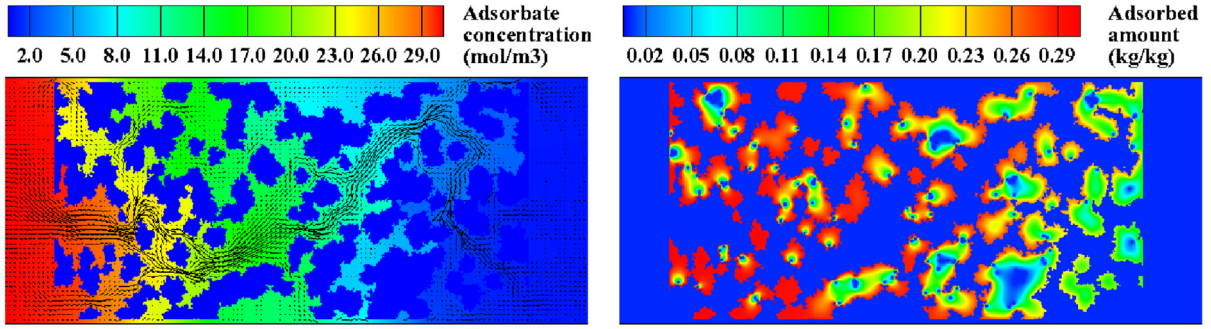

(b) Structure $P2$: ε =0.580

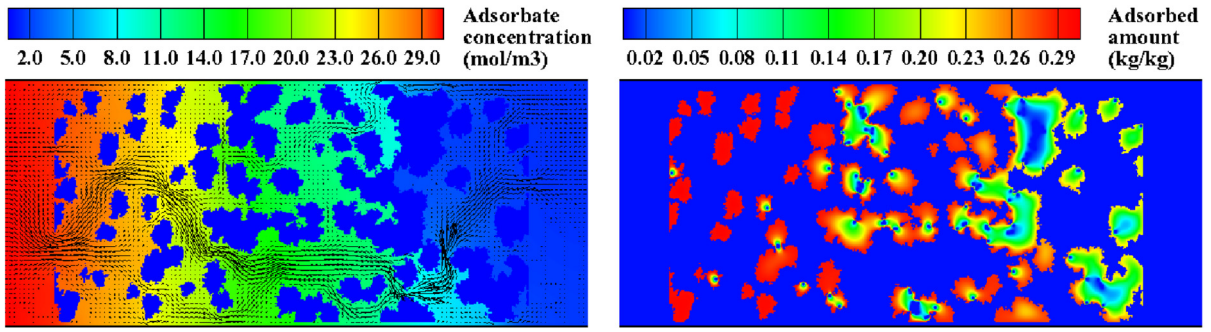

(c) Structure $P3$: ε =0.665

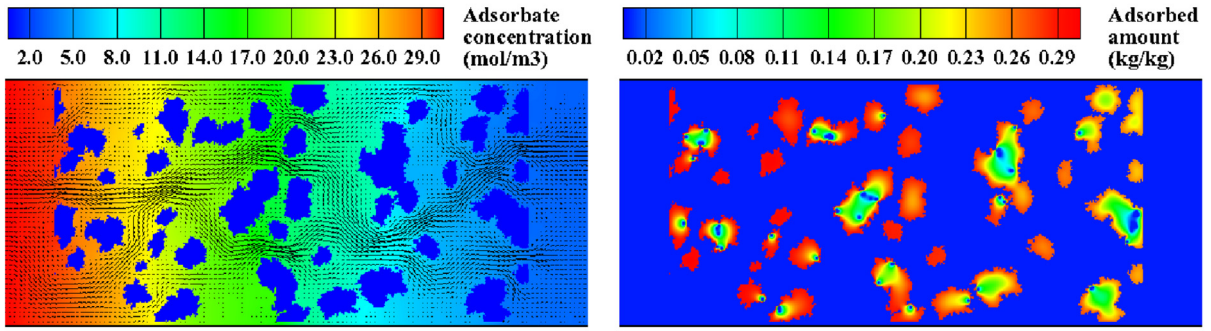

(d) Structure $P4$: ε =0.766

FIG. 6. Results of the transient velocity vector profile and adsorbate concentration contour in bulk fluid (left) as well as the resulting adsorbed amount in porous structures (a) $P1$, (b) $P2$, (c) $P3$, and (d) $P4$, at 510 μs (right). The velocity vectors of the four cases have the same reference length and density.

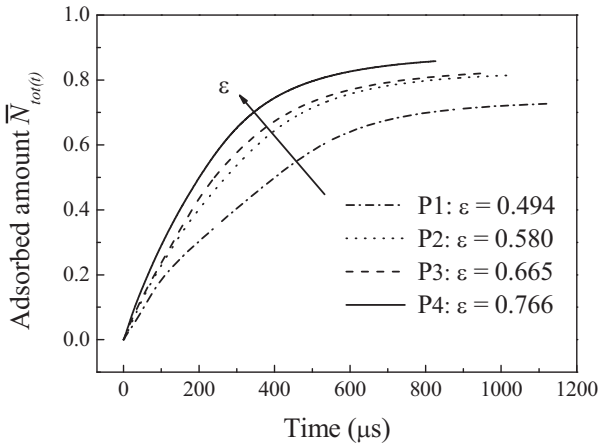

FIG. 7. The time history of the averages of the dimensionless adsorbed amount $\bar{N}_{\mathrm{tot}(t)}$ for structures $P1$, $P2$, $P3$, and $P4$.

Eq. (23). It is determined by calculating the average value of the adsorbed amount among all the computational points of the adsorbent particles at time t. $\bar{N}_{\mathrm{tot}(t)}$ clearly describes the overall performance of the dynamic adsorption process,

$$\overline{N}_{\mathrm{tot}(t)} = \left.\frac{\sum_i \sum_j N_{(t)(i,j)}}{\sum_i \sum_j N_m}\right|_{(i,j)\in \mathrm{particle}}. \tag{23}$$

B. Effect of porosity

The investigated porous media are the four structures ($P1$, $P2$, $P3$, and $P4$ in Table II) under different porosities and the same average particle size of approximately 46 lattice units. Figure 6 presents the transient velocity vector profile and adsorbate concentration contour in the bulk fluid. The figure also depicts the resulting adsorbed amount in the particles of the four structures at 510 μs as an example. With an increased porosity, the velocity vector field becomes increasingly intensive as the vector length increases, thus indicating a fully developed flow field. Accordingly, the contour value of the adsorbate concentration is relatively high at the outlet, thus indicating that the adsorbate proceeds smoothly. In the meantime, the contour of the adsorbed amount is in close proximity to the saturation adsorption state. Figure 7 quantitatively shows the time history of the averages of the dimensionless adsorbed amount $\bar{N}_{\mathrm{tot}(t)}$ of the four structures. The adsorbed amount approaches the steady state as time passes. An early adsorption equilibrium at a high porosity is attributed to the low external mass transfer resistance, which is associated with a fast adsorption rate. In our previous study [41], the effect of the porosity on adsorption processes was researched in porous media with regular arrangements of square particles. The variation trend of adsorbed amount with porosity is similar in the present paper and Ref. [41], whereas the variation trend in the present paper is more evident because the porous geometric morphology and the length-width ratio of the domain are different.

Figures 8(a) and 8(b) show the lattice permeability and dimensionless interparticle transfer coefficient D_{trans}/D_s of the four structures, respectively. A large porosity clearly gives rise

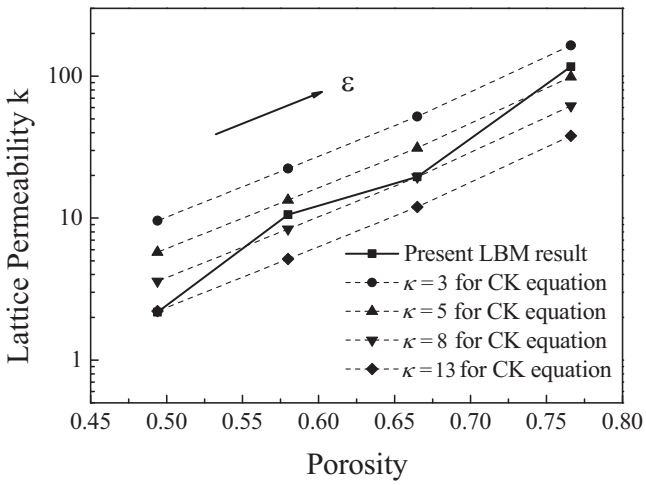

(a)

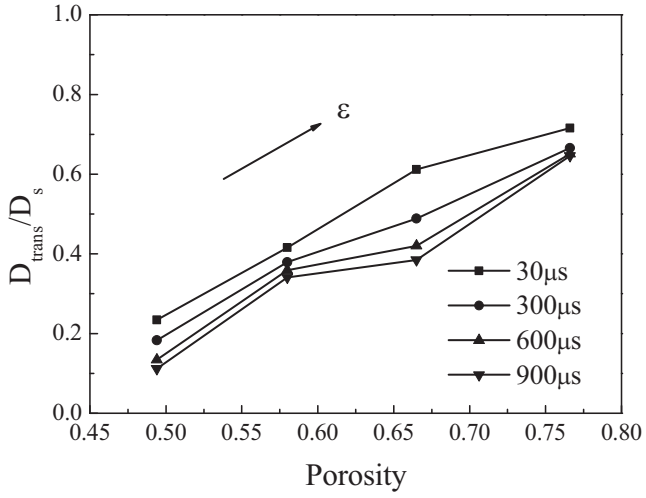

(b)

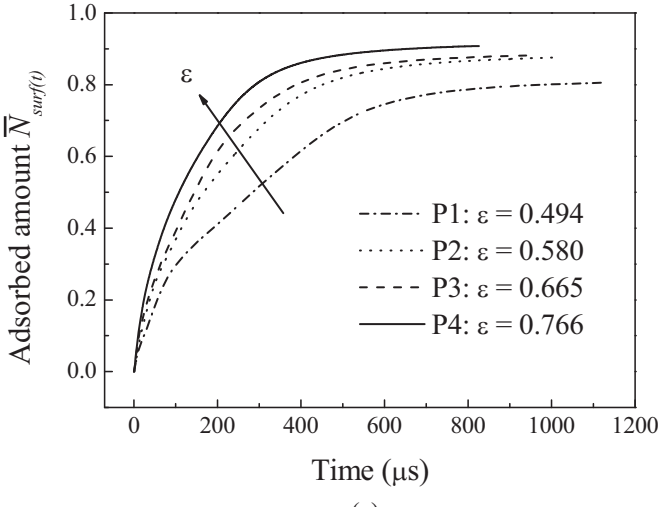

(c)

FIG. 8. Results of (a) lattice permeability, (b) dimensionless interparticle transfer coefficient, and (c) interfacial average of the dimensionless adsorbed amount $\bar{N}_{\mathrm{surf}(t)}$ for structures $P1$, $P2$, $P3$, and $P4$.

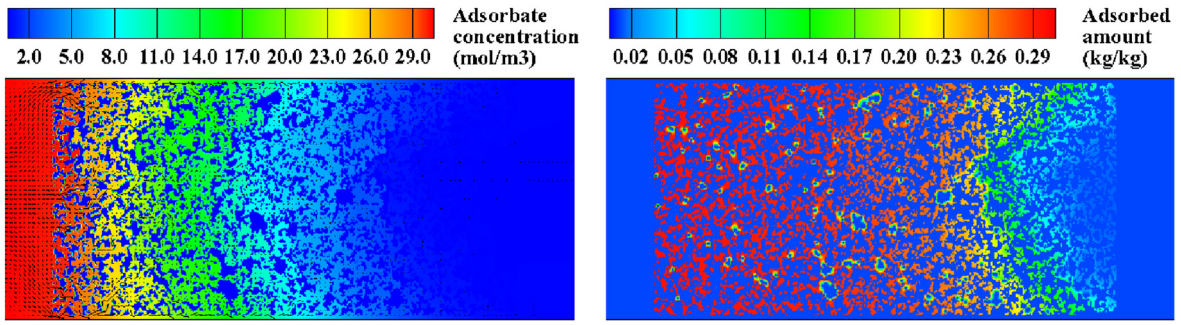

(a) Structure $D1$: d_p=9.69

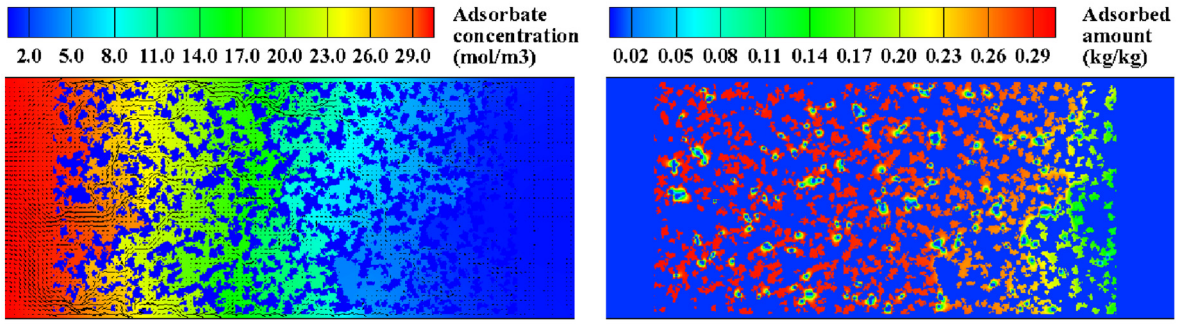

(b) Structure $D2$: d_p=14.82

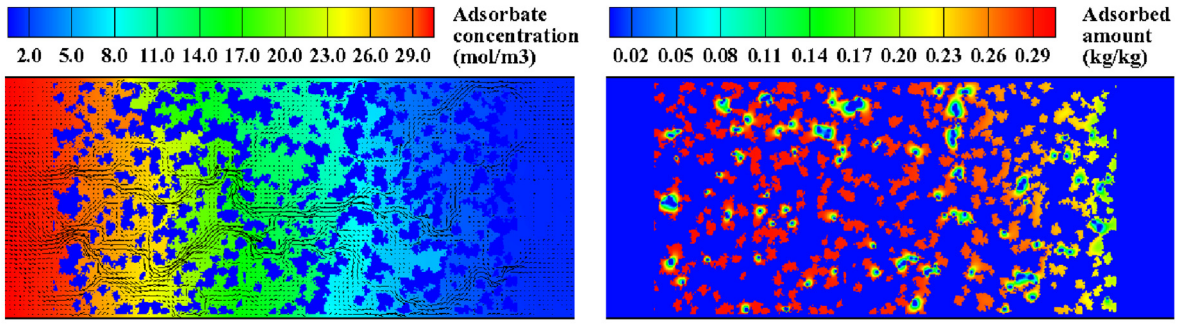

(c) Structure $D3$: d_p=20.86

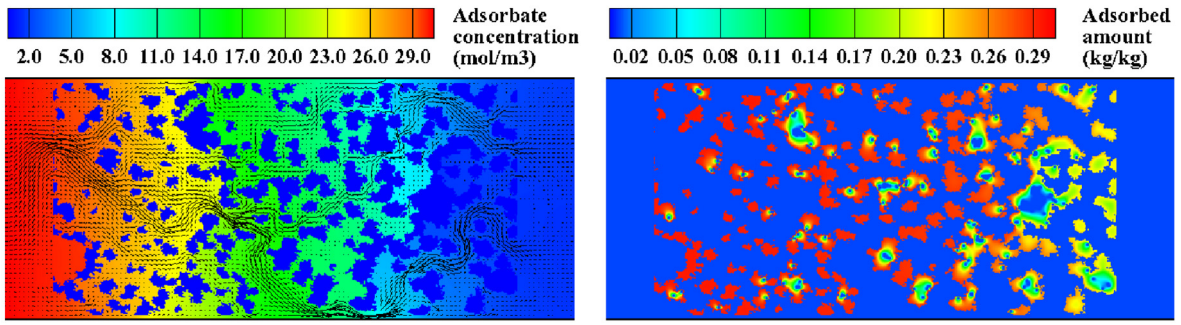

(d) Structure $D4$: d_p=25.72

FIG. 9. Results of the transient velocity vector profile and adsorbate concentration contour in bulk fluid (left) as well as the resulting adsorbed amount in porous structures (a) $D1$, (b) $D2$, (c) $D3$, (d) $D4$, (e) $D5$, (f) $D6$, (g) $D7$, and (h) $D8$ at 510 μs (right). The velocity vectors of the eight cases have the same reference length and density.

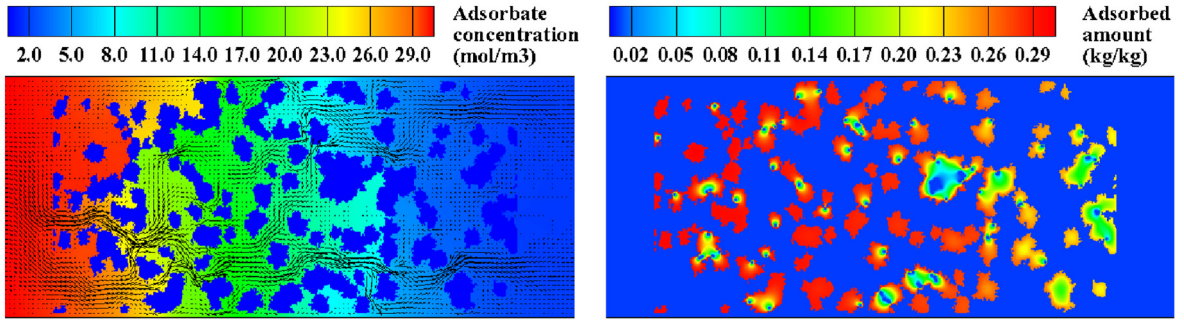

(e) Structure $D5$: d_p=35.48

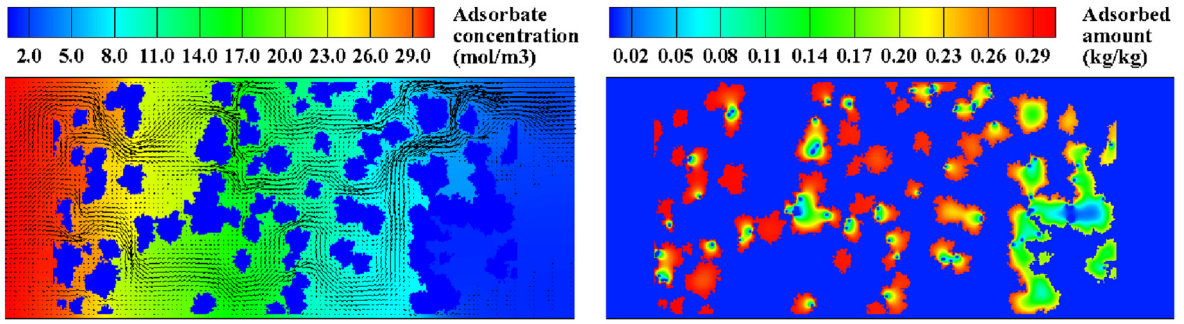

(f) Structure $D6$: d_p=43.25

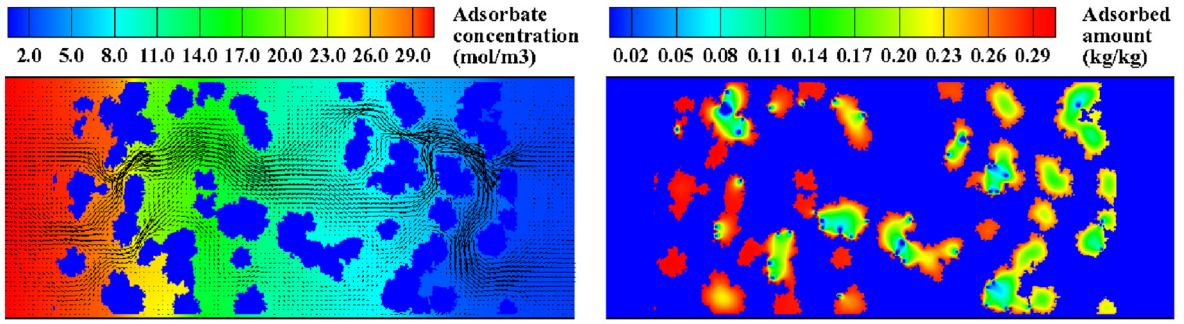

(g) Structure $D7$: d_p=52.08

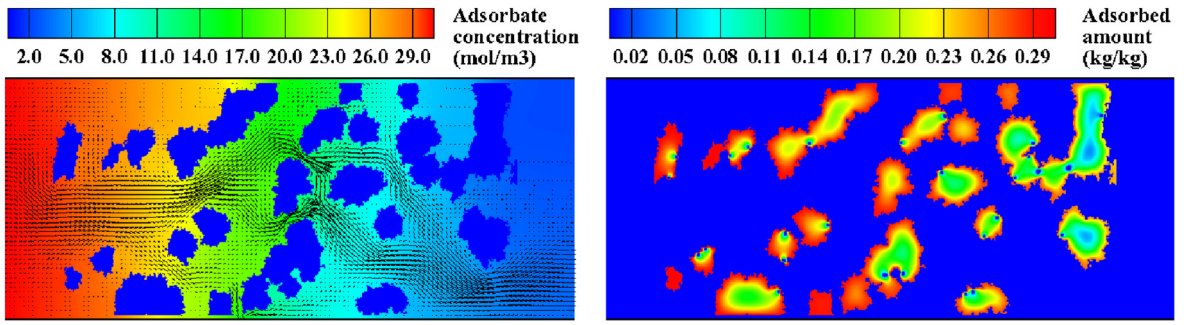

(h) Structure $D8$: d_p=64.55

FIG. 9. (*Continued*).

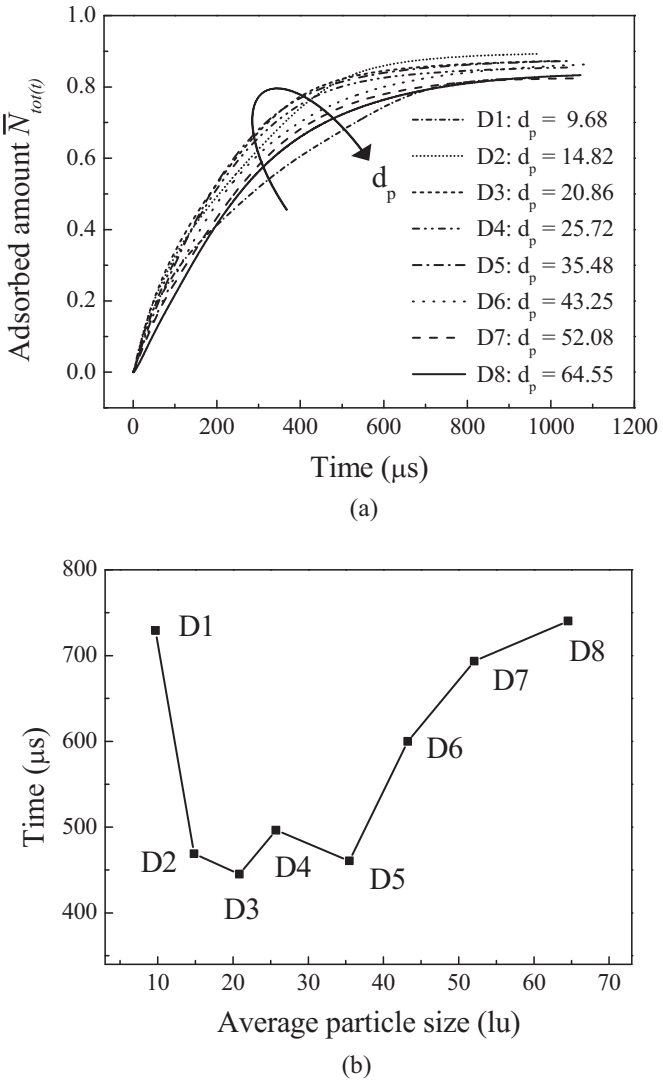

FIG. 10. Results of the (a) time history of the average of the dimensionless adsorbed amount $\bar{N}_{\mathrm{tot}(t)}$ and (b) the required time to reach 80% of the saturated adsorbed amount for structures $D1$, $D2$, $D3$, $D4$, $D5$, $D6$, $D7$, and $D8$.

to a large permeability and interparticle transfer coefficient. This result can be analyzed with the empirical Carman-Kozeny (CK) equation for permeability, which is given as [66]

$$k = \frac{d_p^2 \varepsilon^3}{36\kappa(1-\varepsilon)^2}, \tag{24}$$

where κ is the Kozeny constant. As shown in Fig. 8(a), the lattice permeability predicted with the present model and CK equation both increased with increased porosities. The variation trend of the LBM result and CK equation are consistent at different values of κ. In addition, κ varies in the range of 3–13 during the porosity range. This implies that the Kozeny constant can vary with porosity even for the same material [67,68]. As shown in Fig. 8(b), the dimensionless interparticle transfer coefficient gradually decreases as the adsorption reaches to the equilibrium state with elapsed time.

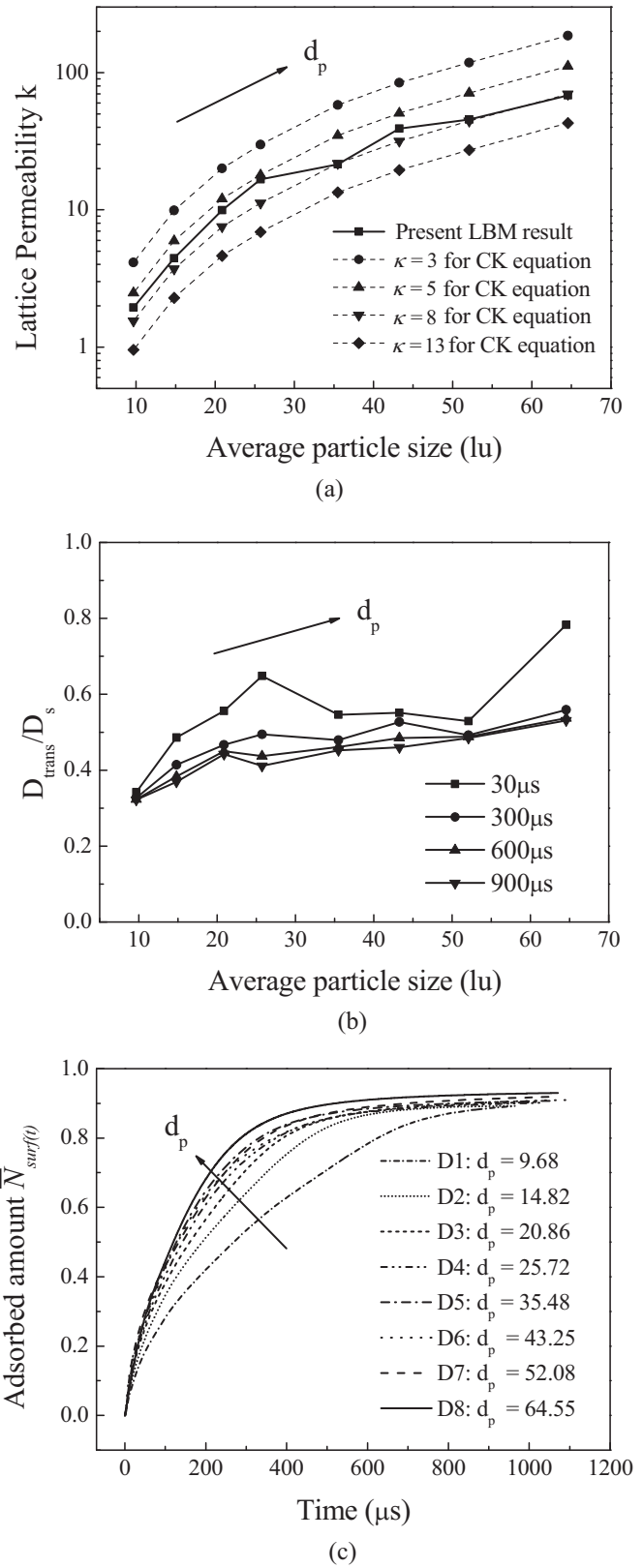

FIG. 11. Results of the (a) lattice permeability, (b) dimensionless interparticle transfer coefficient, and (c) interfacial average of the dimensionless adsorbed amount $\bar{N}_{\mathrm{surf}(t)}$ for structures $D1$, $D2$, $D3$, $D4$, $D5$, $D6$, $D7$, and $D8$.

Furthermore, D_{trans}/D_s increases with an increase in porosity or permeability. This is attributed to that resistance of fluid low and diffusion both decreased with increased porosity. Under this condition, more adsorbates are transferred to the particle surfaces, and the interfacial average of the dimensionless adsorbed amount $\overline{N}_{\text{surf}(t)}$ becomes fully developed as shown in Fig. 8(c). For the intraparticle mass transfer processes, only a slight difference is observed in the resistances of the four structures because they have the same average particle size. Notably, the preceding part is mainly focused on the average adsorbed amount, yet the total adsorbed amount is also related to the adsorbent mass. In practical applications, a large porosity should be prioritized if the adsorbent mass is constant.

C. Effect of average adsorbent particle size

This part investigates the influence of the average adsorbent particle size on the adsorption processes. The porous media are the eight generated structures presented in Table III. These structures have different average particle sizes with the same porosity of about 0.72. Figure 9 shows the profile of the transient velocity vector, the contour of the adsorbate concentration, and the resulting adsorbed amount of the eight structures at 510 μs. As the particle size increases, a fully developed flow field is reached, and the adsorbate concentration proceeds adequately. The adsorbed amount transfers from the particle surfaces to the intraparticles, and its average value decreases along the flow direction.

Figure 10(a) quantitatively presents the time history of the averages of the dimensionless adsorbed amount $\bar{N}_{\text{tot}(t)}$ of the eight structures. The adsorbed amount reaches the equilibrium state as time passes. Notably, as the particle size increases, the time required to reach adsorption equilibrium first decreases and then increases as demonstrated in Fig. 10(b). The time needed to reach 80% of the saturated adsorbed amount falls within a minimum range as in the case from $D2$ to $D5$. The nonmonotonic variation tendency shown in Fig. 10 is attributed to the different dominant effects of the external and internal mass transfer characteristics.

External resistance is dominant in small particles. Figure 11(a) shows that the permeability increases with an increase in particle size as indicated by the CK equation. The Kozeny constant κ is between 5 and 8. This implies that the Kozeny constant κ is more sensitive to porosity than particle size by compared with Fig. 8(a). As shown in Fig. 11(b), the dimensionless interparticle transfer coefficient reduces with elapsed time and increases with increased average particle size. Figure 11(c) shows the interfacial adsorbed amount with time at different particle sizes. The interfacial adsorbed amount also proceeds quickly as particle size increases. Therefore, external resistance decreases as particle size increases to result in an early time for adsorption equilibrium on particle surfaces. However, internal resistance controls the mass transfer efficiency for large particles. The internal mass transfer resistance increases with an increase in particle size to reduce the adsorption rate. Finally, the total mass transfer resistance can reach a minimum point, and the corresponding adsorption rates reach a maximum point at a certain particle size range. The appropriate particle size range is 14.82–35.48 lattice length or 3–7 μm within the preset parameters of the length conversion rule (Table VI).

This effect of particle size is different from that described in the literature [69–71]. Reference [69] used the empirical Ergun's equation to describe the external hydrodynamic effect and incorporated mean porosity into the mass conservation equation to realize the volume averaging method. References [70,71] applied the film resistance model to consider external resistance. The results in Refs. [69–71] show that an increase in particle size leads to a small adsorption rate and, thus, a delayed equilibrium state. The divergence between these previous studies and the present paper lies in the difference among the models of mass transfer resistance. The external mass transfer efficiency is wholly considered in the present pore-scale simulation. This nonmonotone variation trend is also different from the result within our previous studies [41] because of the random porous morphology and larger length-width ratio of the domain.

V. CONCLUSION

The LBM approach is employed to simulate gas-solid adsorption processes in reconstructed random porous adsorbent structures. The interparticle, interfacial, and intraparticle mass transfer characteristics are investigated in detail on the pore scale. The effect of porosity and particle size on dynamic adsorption performance is discussed. The pore-scale simulation reveals the contributions of both the external and internal mass transfer resistances. External resistance is dominant when porosity varies at a fixed particle size. An increase in porosity results in an increase in adsorption rate. External resistance is dominant for small particle sizes, whereas internal resistance controls the mass transport for large particles. A moderate particle size range (3–7 μm) exists and corresponds to a maximum adsorption rate. From the perspective of stochastic reconstruction at the pore-scale level, the present paper can provide both theoretical and practical guidance for the design and optimization of adsorption systems.

ACKNOWLEDGMENTS

This work was supported by the National Natural Science Foundation of China (Grants No. 51322604 and No. 51406009).

[1] R. S. Maier, D. M. Kroll, Y. E. Kutsovsky, H. T. Davis, and R. S. Bernard, Phys. Fluids **10**, 60 (1998).

[2] T. Zeiser, P. Lammers, E. Klemm, Y. W. Li, J. Bernsdorf, and G. Brenner, Chem. Eng. Sci. **56**, 1697 (2001).

[3] D. A. Graf von der Schulenburg and M. L. Johns, Chem. Eng. Sci. **66**, 3003 (2011).

[4] K. N. Grew, A. S. Joshi, A. A. Peracchio, and W. K. S. Chiu, J. Power Sources **195**, 2331 (2010).

[5] D. Beugre, S. Calvo, G. Dethier, M. Crine, D. Toye, and P. Marchot, J. Comput. Appl. Math. **234**, 2128 (2010).
[6] L. Chen, Q. Kang, Y.-L. He, and W.-Q. Tao, Int. J. Hydrogen Energy **37**, 13943 (2012).
[7] R. Machado, Chem. Eng. Sci. **69**, 628 (2012).
[8] D. Hlushkou, F. Gritti, A. Daneyko, G. Guiochon, and U. Tallarek, J. Phys. Chem. C **117**, 22974 (2013).
[9] L.-Z. Zhang, AIChE J. **60**, 3925 (2014).
[10] L. Chen, L. Zhang, Q. Kang, H. S. Viswanathan, J. Yao, and W. Tao, Sci. Rep. **5**, 8089 (2015).
[11] L. Hao and P. Cheng, J. Power Sources **186**, 104 (2009).
[12] T. Rosén, J. Eller, J. Kang, N. I. Prasianakis, J. Mantzaras, and F. N. Büchi, J. Electrochem. Soc. **159**, F536 (2012).
[13] K. Yamamoto, N. Takada, and M. Misawa, P. Combust. Inst. **30**, 1509 (2005).
[14] M. E. Kutay, A. H. Aydilek, and E. Masad, Comput. Geotech. **33**, 381 (2006).
[15] F. Jiang and T. Tsuji, Phys. Rev. E **90**, 053306 (2014).
[16] S. P. Sullivan, F. M. Sani, M. L. Johns, and L. F. Gladden, Chem. Eng. Sci. **60**, 3405 (2005).
[17] C. Chukwudozie and M. Tyagi, AIChE J. **59**, 4858 (2013).
[18] Z. Chai, B. Shi, J. Lu, and Z. Guo, Comput. Fluids **39**, 2069 (2010).
[19] L. W. Rong, K. J. Dong, and A. B. Yu, Chem. Eng. Sci. **99**, 44 (2013).
[20] Q. Ma, Z. Chen, J. Shi, and D. Li, Build. Environ. **72**, 145 (2014).
[21] Z.-X. Tong, Y.-L. He, L. Chen, and T. Xie, Comput. Fluids **105**, 155 (2014).
[22] J. Cai and X. Huai, Appl. Therm. Eng. **30**, 715 (2010).
[23] M. Zhang, G. Ye, and K. V. Breugel, Comput. Mater. Sci. **68**, 142 (2013).
[24] C. Huber, B. Shafei, and A. Parmigiani, Geochim. Cosmochim. Acta **124**, 109 (2014).
[25] Y. Yong, X. Lou, S. Li, C. Yang, and X. Yin, Comput. Math. Appl. **67**, 412 (2014).
[26] Q. Ma and Z. Chen, Int. J. Heat Mass Transfer **79**, 925 (2014).
[27] E. J. Javaran, S. A. G. Nassab, and S. Jafari, Int. J. Therm. Sci. **49**, 1031 (2010).
[28] A. Grucelski and J. Pozorski, Comput. Fluids **71**, 406 (2013).
[29] D. d'Humières, I. Ginzburg, M. Krafczyk, P. Lallemand, and L.-S. Luo, Philos. Trans. R. Soc., A **360**, 437 (2002).
[30] P. Lallemand and L.-S. Luo, Phys. Rev. E **61**, 6546 (2000).
[31] P. Lallemand and L.-S. Luo, Phys. Rev. E **68**, 036706 (2003).
[32] J. Latt and B. Chopard, Math. Comp. Sim. **72**, 165 (2006).
[33] O. Malaspinas, arXiv:1505.06900.
[34] K. K. Mattila, L. A. Hegele, and P. C. Philippi, Phys. Rev. E **91**, 063010 (2015).
[35] I. V. Karlin, A. Ferrante, and H. C. Öttinger, Europhys. Lett. **47**, 182 (1999).
[36] I. V. Karlin, F. Bösch, and S. S. Chikatamarla, Phys. Rev. E **90**, 031302 (2014).
[37] D. Ricot, S. Marié, P. Sagaut, and C. Bailly, J. Comput. Phys. **228**, 4478 (2009)
[38] N. Manjhi, N. Verma, K. Salem, and D. Mewes, Chem. Eng. Sci. **61**, 7754 (2006).
[39] N. Verma, K. Salem, and D. Mewes, Chem. Eng. Sci. **62**, 3685 (2007).
[40] M. Levesque, M. Duvail, I. Pagonabarraga, D. Frenkel, and B. Rotenberg, Phys. Rev. E **88**, 013308 (2013).
[41] L. Zhou, Z. G. Qu, L. Chen, and W. Q. Tao, J. Comput. Phys. **300**, 800 (2015).
[42] M. H. Chahbani, J. Labidi, and J. Paris, Appl. Therm. Eng. **22**, 23 (2002).
[43] M. Wang, J. Wang, N. Pan, and S. Chen, Phys. Rev. E **75**, 036702 (2007).
[44] H. Liu, A. J. Valocchi, Q. Kang, and C. Werth, Transp Porous Media **99**, 555 (2013).
[45] R. B. Bird, W. E. Stewart, and E. N. Lightfoot, *Transport Phenomena,* 2nd ed. (Wiley, New York, 2002).
[46] A. Ghassemi and A. Pak, Int. J. Numer. Anal. Methods Geomech. **35**, 886 (2011).
[47] M. Cheng and L.-S. Luo, Phys. Fluids **19**, 063601 (2007).
[48] I. Ginzburg and D. d´Humières, Phys. Rev. E **68**, 066614 (2003).
[49] Z. Guo, C. Zheng, and B. Shi, Phys. Fluids **14**, 2007 (2002).
[50] M. Yoshino and T. Inamuro, Int. J. Numer. Methods Fluids **43**, 183 (2003).
[51] X. Shan, X.-F. Yuan, and H. Chen, J. Fluid Mech. **550**, 413 (2006).
[52] P. C. Philippi, L. A. Hegele, Jr., L. O. E. dos Santos, and R. Surmas, Phys. Rev. E **73**, 056702 (2006).
[53] D. N. Siebert, L. A. Hegele, R. Surmas, L. O. E. Santos and P. C. Philippi, Int. J. Mod. Phys. C **18**, 546 (2007).
[54] X. Shan, Phys. Rev. E **81**, 036702 (2010).
[55] A. Nabovati and A. C. M. Sousa, in *New Trends in Fluid Mechanics Research*, edited by F. G. Zhuang and J. C. Li (Springer, Berlin/Heidelberg, 2009), pp. 518.
[56] A. Koponen, M. Kataja, and J. Timonen, Phys. Rev. E **54**, 406 (1996).
[57] I. Ginzburg, F. Verhaeghe, and D. d´Humières, Commun. Comput. Phys. **3**, 427 (2008).
[58] D. d'Humières and I. Ginzburg, Comput. Math. Appl. **58**, 823 (2009).
[59] H. Cho, N. Jeong, and H. J. Sung, Int. J. Heat Fluid Flow **44**, 435 (2013).
[60] A. Narváez, T. Zauner, F. Raischel, R. Hilfer, and J. Harting, J. Stat. Mech. (2010) P11026.
[61] C. Manwart, U. Aaltosalmi, A. Koponen, R. Hilfer, and J. Timonen, Phys. Rev. E **66**, 016702 (2002).
[62] M. Bouzidi, M. Firdaouss, and P. Lallemand, Phys. Fluids **13**, 3452 (2001).
[63] P. Lallemand and L.-S. Luo, J. Comput. Phys. **184**, 406 (2003).
[64] C. Pan, L.-S. Luo, and C. T. Miller, Comput. Fluids **35**, 898 (2006).
[65] L. Chen, H.-B. Luan, Y.-L. He, and W.-Q. Tao, Int. J. Therm. Sci. **51**, 132 (2012)
[66] P. C. Carman, Chem. Eng. Res. Des. **75**, S32 (1997).
[67] P. Xu and B. Yu, Adv. Water Resour. **31**, 74 (2008).
[68] A. E. Khabbazi, J. S. Ellis, and A. Bazylak, Comput. Fluids **75**, 35 (2013).
[69] İ. Solmuş, D. A. S. Rees, C. Yamalı, D. Baker, and B. Kaftanoğlu, Int. J. Refrig. **35**, 652 (2012).
[70] P. R. Jena, S. De, and J. K. Basu, Chem. Eng. J. **95**, 143 (2003).
[71] Z. Al-Qodah, A. T. Shawaqfeh, and W. K. Lafi, Adsorption **13**, 73 (2007).